Journal of the European Ceramic Society 36 (2016) 2611–2626

Contents lists available at www.sciencedirect.com

Journal of the European Ceramic Society

journal homepage: www.elsevier.com/locate/jeurceramsoc

$CaZrO_3$–MgO structural ceramics obtained by reaction sintering of dolomite-zirconia mixtures

Fernando Booth[a,b], Liliana Garrido[b], Esteban Aglietti[b], Abílio Silva[a,c], Pilar Pena[a], Carmen Baudín[a,*]

[a] Instituto de Cerámica y Vidrio, ICV-CSIC, Kelsen 5, 28049 Madrid, Spain
[b] CETMIC (Centro de Tecnología de Recursos Minerales y Cerámica, CIC-CONICET La Plata), Camino Centenario y 506, C.C.49 (B1897ZCA) M.B. Gonnet, Buenos Aires, Argentina
[c] C-MAST, Department of Electromechanical Engineering, University of Beira Interior, 6201-001 Covilhã, Portugal

ARTICLE INFO

Article history:
Received 9 February 2016
Received in revised form 17 March 2016
Accepted 21 March 2016
Available online 1 April 2016

Keywords:
$CaZrO_3$
Dolomite
Reaction sintering
Phase equilibrium diagrams
Structural applications

ABSTRACT

Processing and properties of two fine grain and dense $CaZrO_3$-MgO based composites obtained by reaction sintering of pure ZrO_2 and dolomite ($CaMg(CO_3)_2$) are described. Two dolomites with different levels of impurities were used to fabricate the materials: high purity (impurity content ≈1.2 wt.%, material DBZ) and impure dolomite (impurity content ≈6.12 wt.%, material DNZ). Mixtures (molar 1:1) were attrition milled and the reaction and sintering processes were studied using dynamical techniques (DTA-TG and dilatometry). Adequate sintering schedule was selected using the controlled sintering technique. The role of impurities on the physical characteristics, microstructure and mechanical properties of the obtained composites was analysed. Noticeable changes in microstructure, porosity, grain size and phases, were observed as function of final sintering temperature at 1350, 1400, 1450 °C, and impurity content. The obtained microstructures are discussed on the basis of the phase equilibrium relationships.

1. Introduction

Calcium zirconate ($CaZrO_3$, CZ) and periclase (MgO) present high melting points (2365 and 2827 °C for $CaZrO_3$ and MgO, respectively). Moreover, minimum temperature for liquid formation in mixtures of these compounds will be that of the eutectic point of the binary $CaZrO_3$-MgO system, 2060 °C [1,2]. Zirconia (ZrO_2) also presents high melting point (2750 °C) and is solid state compatible with $CaZrO_3$ and MgO [1,2]. First liquid formation in ZrO_2-$CaZrO_3$-MgO mixtures is expected at the relatively high temperature of the ternary ZrO_2-MgO-CaO eutectic point, 1982 °C [1,2].

$CaZrO_3$ presents a crystalline average thermal expansion coefficient (α average between 298 and 1675 K ≈ 10.4×10^{-6} K^{-1}) [3] and thermal conductivity (K ≈ 2–2.2 Wm^{-1} K^{-1}, from 500 to 1500 K [4], similar to yttria fully stabilized zirconia (YFSZ), (Y_2O_3) 0.08 (ZrO_2) 0.92 (YFSZ, $\alpha_{300-1000\ °C} \approx 10 \times 10^{-6}$ $°C^{-1}$ [5], $K \approx 2–2.3$ Wm^{-1} K^{-1}, from 300 to 1500 K [6]). Therefore, $CaZrO_3$ (CZ) materials can be considered as substitutes of YFSZ in structural applications. In fact, $CaZrO_3$ has already been proposed as potential candidate for thermal barrier coatings (TBC) [7,8].

CaO full stabilized zirconia presents thermal properties (α average between 273 and 1275 K ≈ 6×10^{-6} K^{-1} [9], K ≈ 2–2.2 Wm^{-1} K^{-1}, from 500 to 1500 K [4]) similar to those of YFSZ and MgO presents a higher thermal expansion coefficient than both CZ and YFSZ ($\alpha_{25-1000\ °C} \approx 13.5 \times 10^{-6}$ K^{-1} [10], K ≈ 8.1–29.4 Wm^{-1} K^{-1}, from 400 to 1300 K [11]). Therefore, CZ-CaFSZ-MgO composites would also be good candidates for TBC, with even better behaviour in terms of thermal expansion mismatch with metals.

Solid state synthesis of $CaZrO_3$ from CaO and ZrO_2 occurs from temperatures ~900 °C [12]. As it is associated with a significant volume increase (~11%), it is difficult to obtain composites with an adequate degree of densification [13]. Moreover, as main mass transfer mechanism is the diffusion of Ca^{2+} ions through the newly-created $CaZrO_3$, relatively high temperatures would be needed to avoid the presence of free lime in the material [14].

An alternative proposal is that of $CaZrO_3$-based composites fabricated by reaction sintering of ZrO_2 and dolomite ($CaMg(CO_3)_2$) mixtures, that will produce CZ-YFSZ-MgO materials. Decomposition of dolomite at temperatures higher than 800 °C originates highly reactive nanometric particles of CaO, which readily react with ZrO_2 [15]. Thus, final materials without free lime and, consequently, stable against atmospheric moisture would be formed.

* Corresponding author.
E-mail address: cbaudin@icv.csic.es (C. Baudín).

http://dx.doi.org/10.1016/j.jeurceramsoc.2016.03.027
0955-2219/

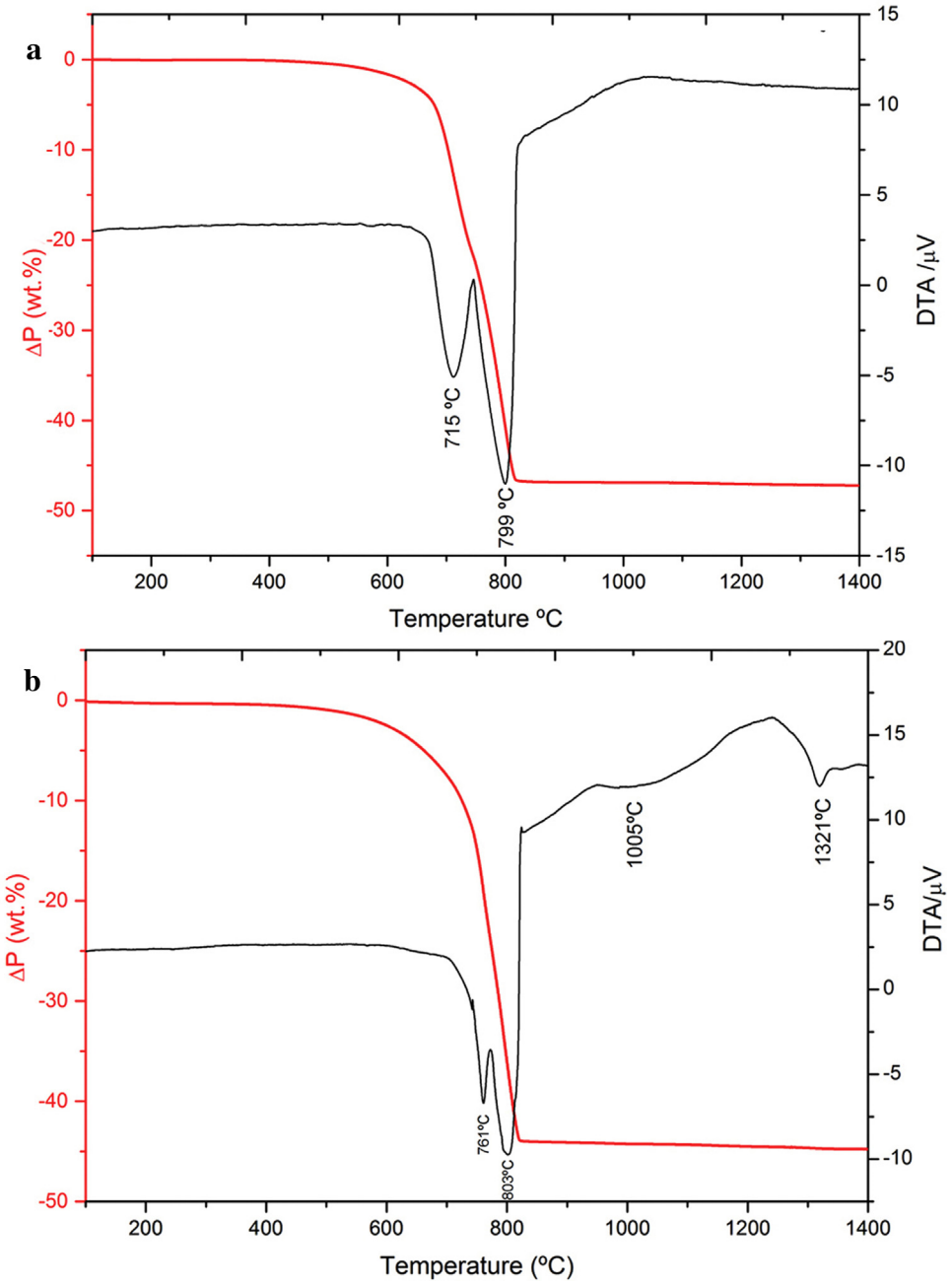

Fig. 1. Differential and thermogravimetric thermal analyses (DTA-TG) of the natural dolomites used. (a) DB. (b) DN.

Reaction takes place according to Eq. (1):

$$(1 + x)ZrO_2 + CaMg(CO_3)_2 \rightarrow MgO + CaZrO_3 + xc\text{-}ZrO_2ss + 2CO_2 \quad (1)$$

Szczerba and Pedzich [13] have used this approach for obtaining $CaZrO_3$-MgO composites. They used two relatively pure dolomites with total amounts of main impurities (SiO_2, Fe_2O_3 and Al_2O_3) of 0.1 and 1.8 wt.%. The natural dolomites were ground and sieved (<63 μm) before mixing with zirconia. A minimum temperature of 1500 °C was needed to complete reaction independently of the firing schedule followed. The maximum density (95% of theoretical) was reached for materials obtained following a two steps process including the pre-calcination of dolomite at 1200 °C. This initial step was proposed to overcome the main problem of using dolomite as raw material which is the extreme mass loss associated to its decarbonation.

These results reveal that, in spite of the formation of highly reactive CaO nanoparticles at low temperature, there are difficulties involved in the use of dolomite-zirconia mixtures to get dense $CaZrO_3$-MgO composites. Such difficulties derive from the expansive character of the formation of $CaZrO_3$ and c-ZrO_2 from dolomite decomposition and reaction with ZrO_2. These processes can lead to abrupt fluctuations of specimen dimensions between 770 and 1270 °C, as observed in constant heating rate experiments [12]. The Rate Controlled Sintering (RCS) technique has been proposed as mean to obtaining dense and fine grained materials (see Ref. [16] for a review). Essentially, this technique consists in designing the heating schedules on the basis of different stages of shrinkage rate. In general, when reactions do not occur in the material, an initial heating stage controlled by a rapid shrinkage rate is desired

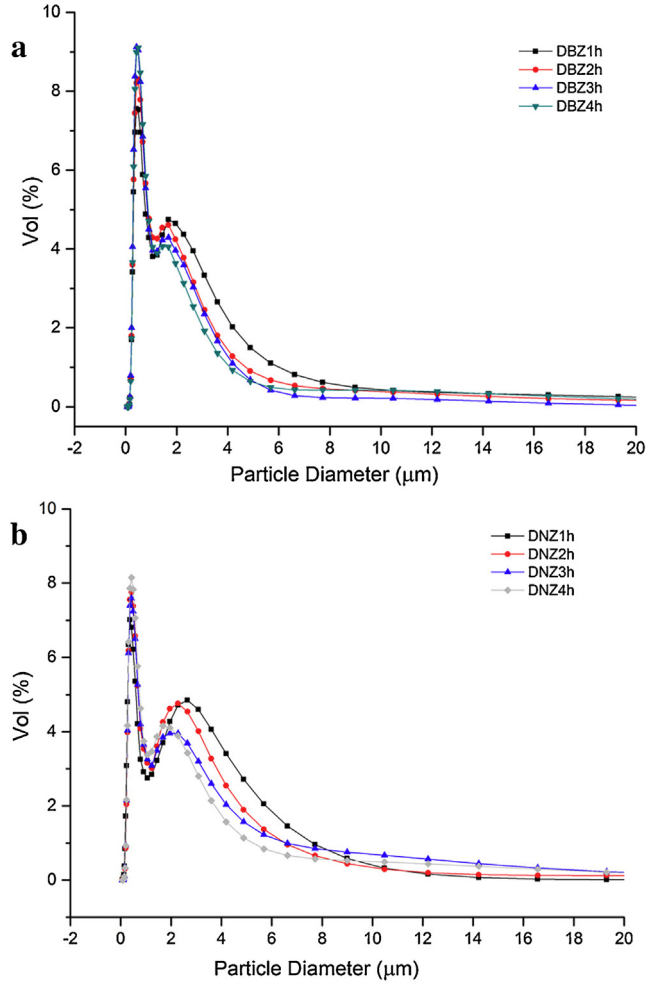

Fig. 2. Effect of milling time on the particle size distribution of the studied dolomite—zirconia mixtures. (a) Composition DBZ. (b) Composition DNZ.

to avoid surface diffusion an associated early grain growth. However, in reactive systems it has been proposed, and successfully applied, the control of the reaction rate in order to obtain a fully reacted and homogeneous microstructure [17]. Reaction rate can be determined by any measurable effect of the reaction.

In this work, the possibility of obtaining by RCS of natural dolomite and zirconia, fine grained and dense $CaZrO_3$-MgO based composites to be used as structural materials is investigated. It is hypothesized that the use of a heating schedule for maintaining a constant shrinkage rate, during the heating stage of the thermal treatment, would minimise the deleterious effect of the dimensional changes within the specimen due to the initial reactions.

Two natural dolomites with different chemical and mineralogical compositions were used as starting powders in order to analyse the effect of impurities on the reaction sintering process and the characteristics of the final composites. Phase content and microstructural development of the resulting materials as function of the final temperature of treatment and the associated mechanical behaviour in terms of hardness and strength have been assessed.

2. Experimental

Commercially available high purity (99.9 wt.%) monoclinic ZrO_2 powder (Saint Gobain-Zir Pro, China) and two natural Argentine dolomites (DB and DN) with different chemical and mineralogical compositions were used as starting materials.

Chemical analysis of the dolomites was carried out using X-ray fluorescence equipment (MagiX PW 2424, Philips, The Netherlands). Specimens were prepared from ground powder with added Li_2B4O_7 following the standard procedure for fused pellets at 1000 °C.

Particle size distribution was measured by a laser scattering method (Malvern, United Kingdom).

Two series of ceramics (DBZ and DNZ) were prepared using ZrO_2-dolomite mixtures with molar ratio 1:1. The adequate amounts of powders to fulfil Eq. (1) were calculated taking into account the chemical composition of the dolomites previously determined.

Homogeneous and fine grained ZrO_2-dolomite mixtures were prepared by attrition milling during 4 h using isopropyl alcohol as media and Y_2O_3-PSZ balls of 1 mm diameter with a powder/balls weight ratio of 1/10. Optimum milling time was determined by analysing the particle size distributions of the powder after milling during 1, 2, 3 and 4 h. After drying at 60 °C for 24 h, the powder was sieved (65 μm) and uniaxially pressed at 20 MPa into discs of ≈10 mm diameter and ≈8 mm height.

The optimum heating schedule for sintering in an electric furnace in air (Termiber, Spain) was established using a combination of thermal analysis and dynamic sintering experiments.

Differential thermal analysis, DTA, and thermogravimetric analysis, TG (STA 409, Netzsch, Germany) at a heating rate of 5 °C/ min up to 1450 °C were used to identify the reactions taking place in the materials. Shrinkage rate-controlled sintering experiments at 0.07 min^{-1} were performed on blocks (≈4 mm × 4 mm) machined from the pressed cylinders in a differential dilatometer (Setsys Evolution, Setaram, France); a constant heating rate at 5 °C/min was imposed until detectable shrinkage occurred in the compacts.

An optimised heating schedule suitable for both compositions was established. It was constituted by three stages at three different constant heating rates: 5 °C/min from room temperature to 600 °C, 2 °C/min from 600 °C to 1270 °C and 1 °C/min from 1270 °C to the maximum temperature. A series of specimens were fabricated for mineralogical and microstructural analysis using this optimized schedule followed by isothermal treatments at 1350 °C, 1400 °C and 1450 °C, during 2 h, and then cooling at 10 °C/min.

Identification of crystalline phases in the sintered ceramics was performed by X-ray Diffraction (XRD) using a diffractometer (Kristalloflex D-5000, Siemens, Germany) with Cu-Kα radiation and a secondary curved graphite monochromator. The X-ray tube operated at 40 kV at 30 mA. Data were collected between 10 and 80° (2θ) with the Bragg–Brentano (θ/2θ) vertical geometry (flat reflection mode).

The XRD diffractograms of the raw materials were analysed using the following ASTM files: PDF 36–0426, for dolomite ($CaMg(CO_3)_2$); PDF 83–0577, for calcite; PDF 46–1045, for quartz (SiO_2); PDF 46–1045, for feldspar ($(K,Na)Al(Si,Al)Si_2O_8$). For the sintered samples, the used ASTM files were: 35–0790, for calcium zirconate ($CaZrO_3$); 071–1176, for magnesia (MgO); 026–0341, for calcia fully stabilized cubic zirconia ($c\text{-}Ca_{0.5}Zr_{0.85}O_{1.85}$); 35–0591, for merwinite ($Ca_3Mg(SiO_4)_2$); 072–0458, for monticellite ($MgCaSiO_4$); 031–0297, for dicalcium silicate (C_2S,Ca_2SiO_4).

The crystalline phase contents of the materials (wt.%) were quantitatively determined using the Rietveld method of refinement. The theoretical densities of the materials were calculated from the theoretical densities (XRD files) and the volume fractions of the constituent phases.

The bulk density and the open porosity of sintered specimens were determined following the procedures described in EN 1389:2003 and the relative densities (RD) of the composites, were calculated as the ratio between bulk and theoretical densities. Total porosity (P) was calculated as: P = 1-RD. Microstructural characterization of the materials was carried out on diamond polished

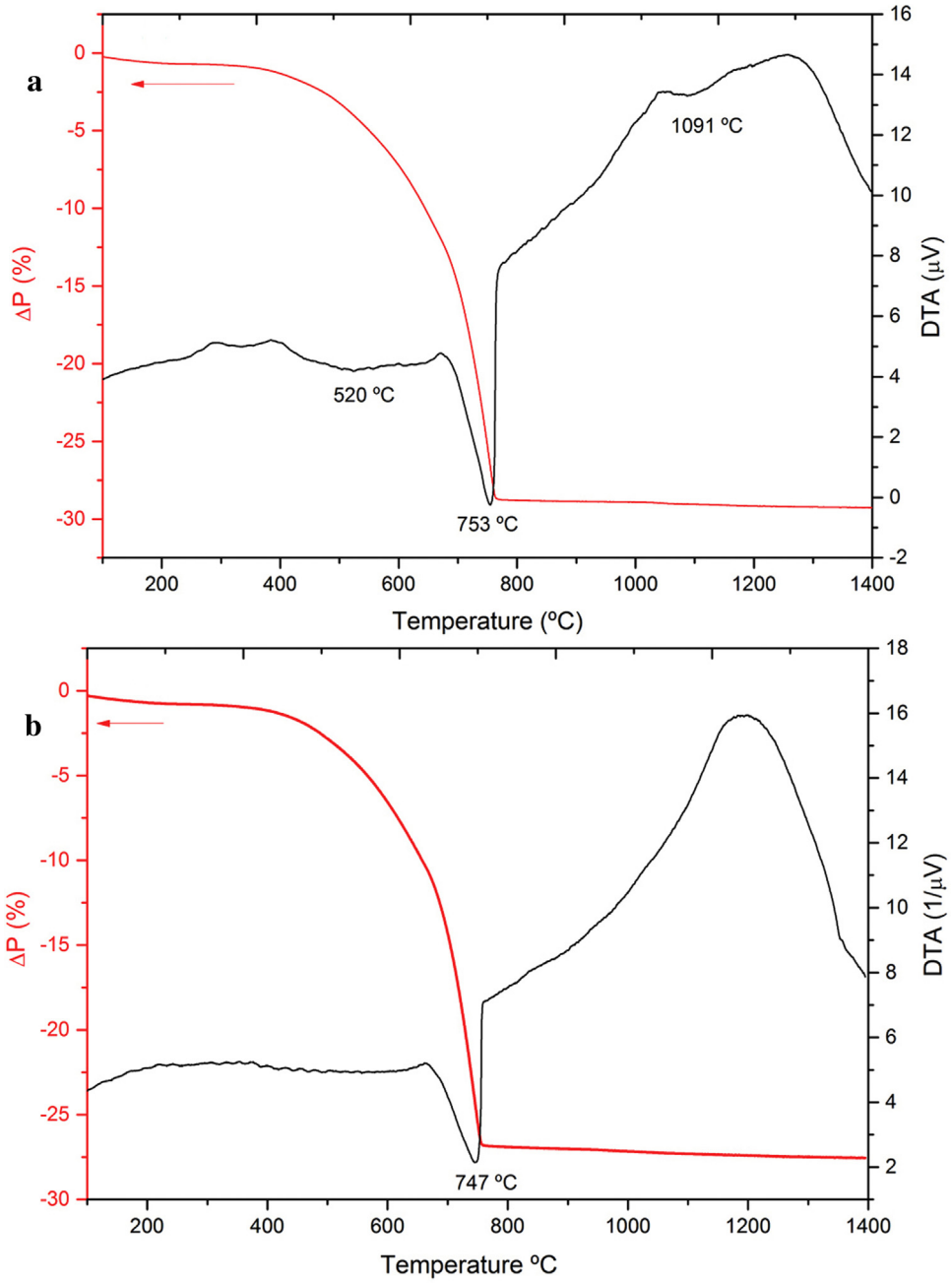

Fig. 3. Differential and thermogravimetric thermal analyses (DTA-TG) of the two studied $CaMg(CO_3)_2$-ZrO_2 mixtures heated at 5 °C/min (a) DBZ. (b) DNZ.

surfaces (down to 3 μm). Scanning electron microscopy (SEM, Hitachi TM-1000, Japan) was performed on "as polished" surfaces. Further microstructural characterisation was performed on polished and Ag-coated specimens using a Field Emission Scanning Electron Microscope, FE-SEM, with analysis by energy dispersive X-ray spectroscopy (EDS) (Hitachi, S-4700 type I, Japan).

Vickers hardness of the materials was evaluated on polished surfaces according to standard ASTM C-1327, averaging 10 measurements per material. Given errors are the standard deviations.

Strength of the materials sintered at 1400 °C was determined by the Diametral Compression of Discs Test (DCDT) following the procedure described elsewhere [18]. Circular discs of diameter (D) ≈7 mm and thickness (t) ≈4 mm, (t/D ≈ 0.6) were tested in a universal testing machine (Microtest, Madrid, Spain) at a frame displacing rate of 0.5 mm/min. In this test the highest tensile strength is uniform across the central part of the diametrical plane of the specimens, being the zones closest to the loading supports in compression. Failure occurs through the diametrical plane and the specimens are broken in two similar pieces.

Strengths, σ_f, were calculated using Eq. (2):

$$\sigma_f = \frac{2F}{\pi Dt} \tag{2}$$

where F is the maximum load. Results of fifteen valid tests were used to calculate the Weibull parameters using the procedure of ENV-843-5 (Aenor, 2006), which involves the simplest form of the Weibull function (Eq. (3)), where P_f is the probability of failure at the stress σ_f (Eq. (2)), σ_0 is the stress at which the probability of failure is 63.2%, called characteristic strength, and m is the Weibull modulus.

$$P_f = 1 - \exp\left[-\left(\frac{\sigma_f}{\sigma_0}\right)^m\right] \tag{3}$$

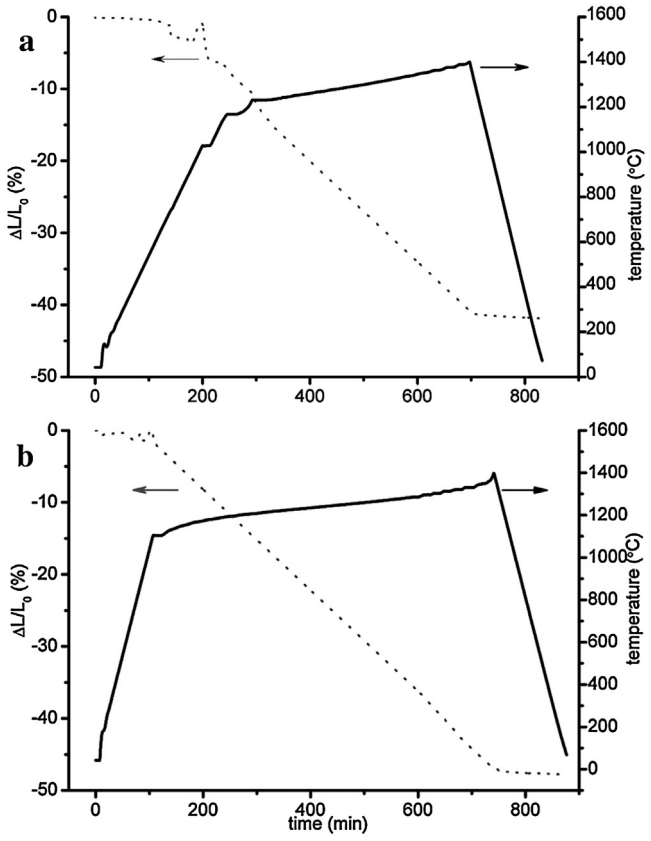

Fig. 4. Compact shrinkage, ΔL/L0 (%), and temperature versus time for the constant rate of shrinkage (0.07/min) experiments. (a) DBZ green compact. (b) DNZ green compact. (For interpretation of the references to colour in this figure legend, the reader is referred to the web version of this article.)

The probability of failure was calculated using Eq. (4):

$$P_f = \frac{n - 0.5}{N} \quad (4)$$

where *N* is the total number of specimens tested and *n* is the specimen rank in ascending order of failure stress.

3. Results

3.1. Raw materials and reaction sintering process

The chemical and mineralogical analyses of the starting materials are summarized in Table 1. Calcite was present as minor constituent in the purest material, DB, (≈1.2 wt.% of impurities) in which main impurities were Al_2O_3 and SiO_2. Quartz and potassium feldspar were identified in DN (≈6.12 wt.% of impurities) in which SiO_2, Al_2O_3, Fe_2O_3 and alkalis were present. The feldspar was identified taking into account not only the XRD pattern but also the fact that significant amounts of K_2O were present in DN. The CaO/MgO molar ratios were 1.045 and 1.079 for DB and DN, respectively.

The differential and thermogravimetric thermal analysis (DTA-TG) of the dolomites are plotted in Fig. 1. Two endothermic peaks are observed for both dolomites. The lowest temperature ones are centred at ≈715 and 760 °C for DB and DN, respectively, and the second ones are observed at ≈800 °C for both dolomites. Significant weight losses are associated to these peaks, ≈47 and 44 wt.% for DB and DN, respectively (Fig. 1). For DN, a broad endothermic band between 950 °C and ≈1100 °C is also observed.

The chemical compositions of the mixtures were calculated taking into account the chemical analysis of the raw materials; results are summarised in Table 2.

Fig. 2 shows the particle size distributions of the dolomite-zirconia mixtures for different milling times. All distributions are bimodal with the maximum for the smallest particles located at ≈0.5 μm, the average grain size of the starting m-ZrO_2 powder. In the starting mixtures, the maximums corresponding to the largest sizes were located at 1.7 and 2.6 μm for DBZ and DNZ, respectively, which would correspond to the dolomites. A significant decrease in sizes occurred from 1 to 3 h milling in DBZ; the volume fraction of particles larger than 1.7 μm decreased from 28% (1 h) to 18% (3 h) and remained constant for 4 h milling. For DNZ, the decrease in sizes continued from 3 to 4 h. The volume fraction of particles larger than 2.6 μm decreased from 34% (1 h) to 22% (3 h) and then to 18% (4 h). A milling time of 4 h was selected for conditioning both powder mixtures before sintering in order to avoid potential agglomerations of particles in DBZ. For this milling time, the volume fraction of particles larger than 1.7 μm in DNZ was 30%.

DTA and TG curves for the DBZ and DNZ mixtures are plotted in Fig. 3. Relatively large weight losses occurred in both mixtures, as shown in the TG curves (29.24 and 27.5 wt.% for DBZ and DNZ, respectively). DTA curves for both materials show a broad endothermic band between ≈400 and 700 °C, and a step endothermic peak around 750 °C. For DBZ, an additional endothermic effect centred at 1090 °C was detected in DTA curve.

In Fig. 4 results from the dynamic sintering experiments are plotted. After an initial instability in the evolution of the shrinkage of the compacts at temperatures lower than ≈1000 °C and ≈1100 °C for DBZ and DNZ, respectively, the imposed shrinkage rate was well followed by both compositions. The total shrinkage experienced by the compacts during the initial period was very low (<2% for DBZ and DNZ, respectively) and the heating rate required to approach the imposed schedule was high (≈5 and 10 °C/min for DBZ and DNZ, respectively).

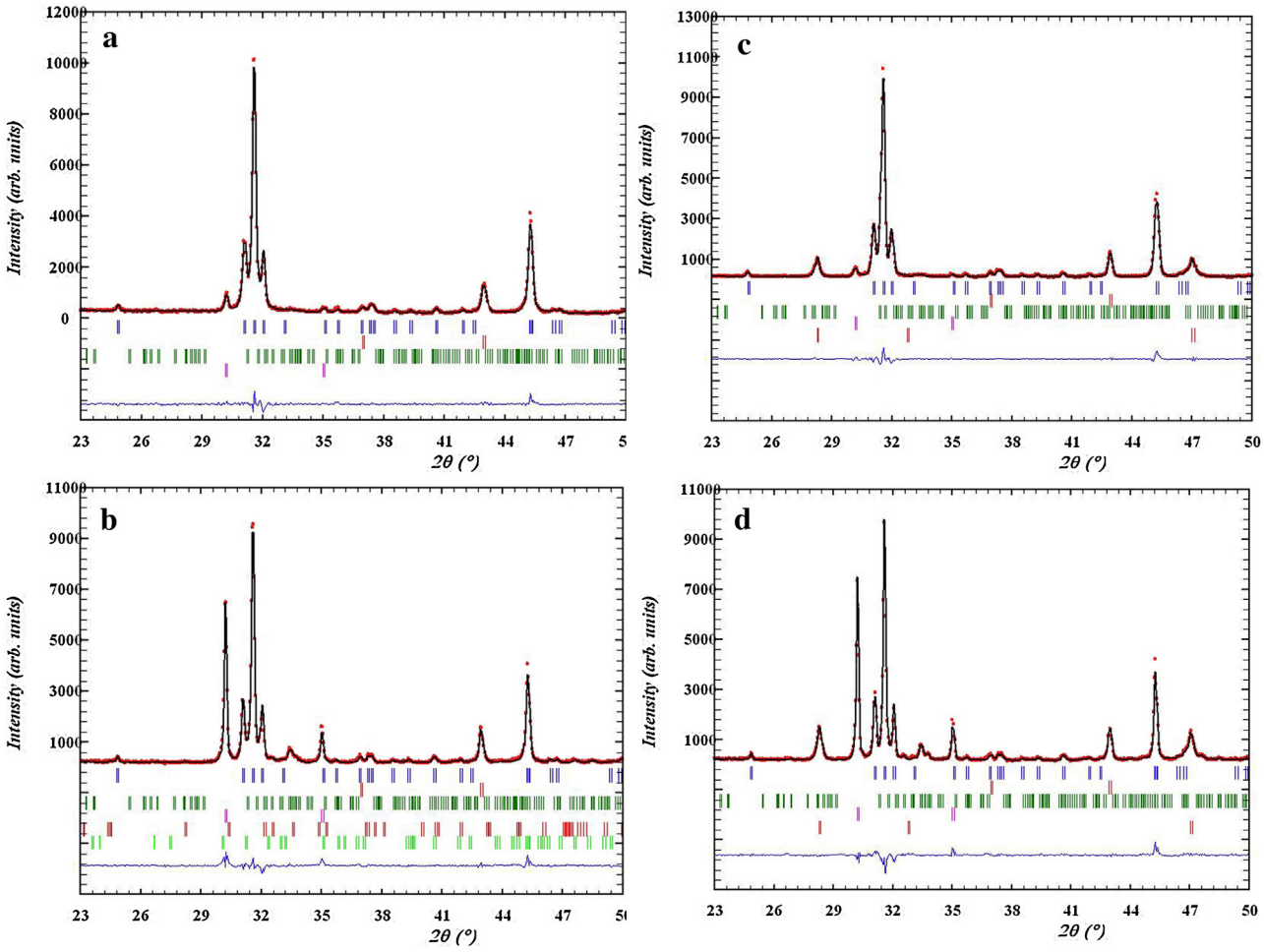

Fig. 5. Characteristic full-prof Rietveld plots (23–50 2θ) for the studied materials sintered at 1450 °C/2 h. The vertical lines mark the Bragg peaks of the phases included in the refinement. Observed (crosses), calculated (line) and difference (bottom line) powder patterns are shown. (a) DBZ. Vertical lines, from top to bottom: $CaZrO_3$, MgO, $CaMg(SiO_3)_2$, c-ZrO_2. (b) DNZ. Vertical lines from top to bottom: $CaZrO_3$, MgO, $CaMg(SiO_3)_2$, c-ZrO_2, and Ca_2SiO_4. (c) DBZ + 15 wt.% CaF_2. Plot used to calculate the amount of amorphous phase. Vertical lines from top to bottom: $CaZrO_3$, MgO, $Ca_3Mg(SiO_4)_2$, c-ZrO_2 and CaF_2. (d) DNZ + 15 wt.% CaF_2. Plot used to calculate the amount of amorphous phase. Vertical lines from top to bottom: $CaZrO_3$, MgO, $Ca_3Mg(SiO_4)_2$, c-ZrO_2 and CaF_2.

Table 1
Chemical analysis (wt.%) of the raw materials used.

	DB		DN		Z
Oxides (wt.%)	original	calcined	original	calcined	m-ZrO_2
Al_2O_3	0.20	0.37	0.50	0.89	–
CaO	31.0	57.7	29.0	51.9	–
Fe_2O_3	0.058	0.107	0.60	1.1	10 ppm
K_2O	<0.02	<0.03	0.50	0.89	–
MgO	21.3	39.7	19.3	34.6	–
SiO_2	1.00	1.86	5.68	10.2	<15 ppm
TiO_2	0.012	0.022	0.025	0.044	<10 ppm
MnO	<0.01	<0.02	0.10	0.18	–
P_2O_5	0.015	0.028	0.013	0.023	–
Na_2O	<0.10	<0.2	<0.10	<0.2	<10 ppm
Cl^-	–	–	–	–	<50 ppm
$ZrO_2(HfO_2)$	–	–	–	–	>99.5 wt.%
Ignition Loss	46.5	–	44.2		0.3 wt.%
Mineralogical analysis	Dolomite Calcite		Dolomite Quartz Feldspar K		Baddeleyite

After this initial period, the temperature-time schedule needed to reach constant shrinkage for DNZ (Fig. 4b) was monotonous and could be simplified by a single slope (≈0.3 °C/min). For DBZ (Fig. 4a), the temperature rate needed from ≈1000 °C to ≈1270 °C was steeper (≈2 °C/min) than for higher temperatures (≈0.4 °C/min).

3.2. Phase composition and microstructure

Characteristic Rietveld plots for both sintered ceramics are shown in Fig. 5a-b as examples. Results of the quantitative Rietveld phase analysis are summarised in Table 3. Major phases in DBZ

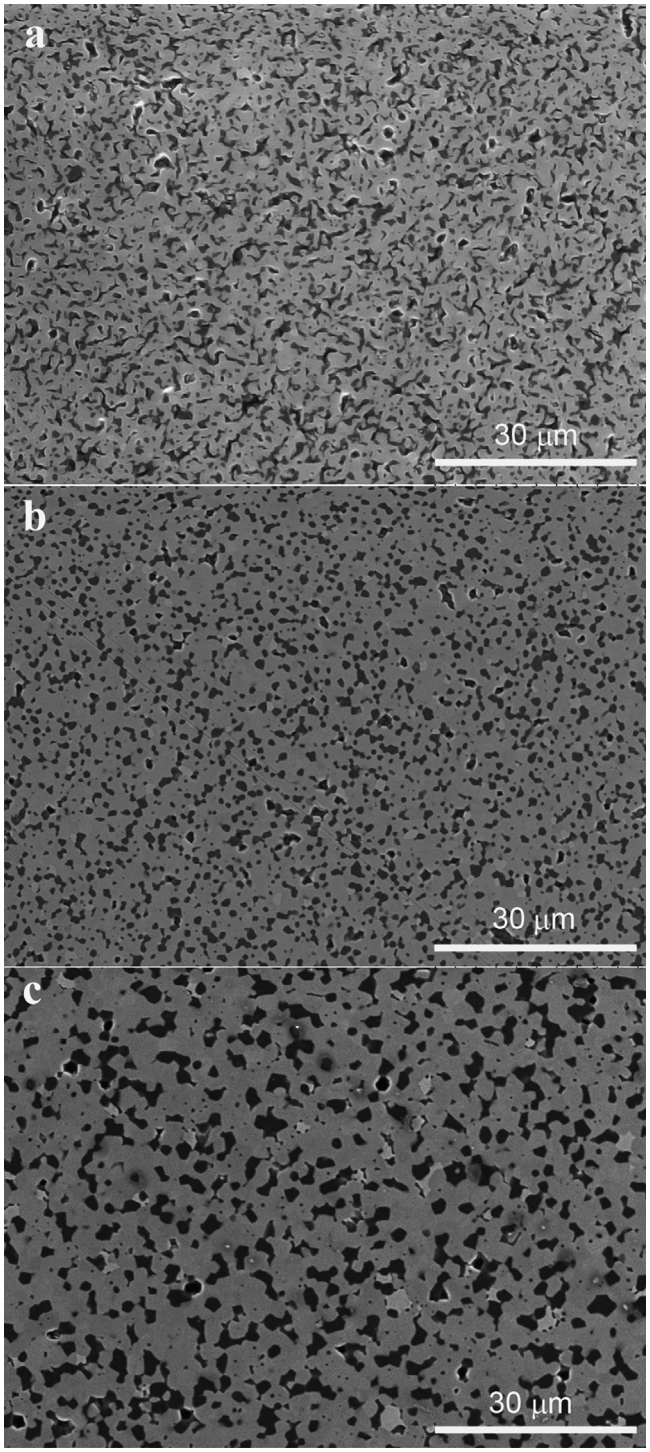

Fig. 6. Characteristic microstructural features of DBZ materials. General aspect of the microstructures observed in scanning electron micrographs of "as polished" surfaces. Common features are a major medium gray phase and a second dark phase. and pores (shinny borders). (a) Material sintered at 1350 °C. Pores (shinny borders) large and of irregular shape are observed. (b) Material sintered at 1400 °C. Irregular shape and round pores (shinny borders) are observed. (c) Material sintered at 1450 °C. A minor phase (light gray) are observed.

were $CaZrO_3$ and MgO; c-ZrO_2 ($Ca_{0.15}Zr_{0.85}O_{1.85}$) and merwinite ($Ca_3Mg(SiO_4)_2$) were present in very low amounts (<4 wt.%) as secondary phases.

There were three major constituents in DNZ materials: $CaZrO_3$, MgO and c-ZrO_2. Merwinite ($Ca_3Mg(SiO_4)_2$), Monticellite ($CaMgSiO_4$) and dicalcium silicate (Ca_2SiO_4) were present as minor phases. Merwinite content increased at 1450 °C whereas monticellite disappeared completely at this temperature. Variations of dicalcium silicate with temperature were inconsistent.

Rietveld analyses to quantify the non-diffracting phases, using 15 wt.% of CaF_2 as internal standard, were performed for the specimens sintered at 1450 °C/2 h (Fig. 5c-d). Values of 4 and 10 wt.% of amorphous phases in DBZ and DNZ, respectively were calculated.

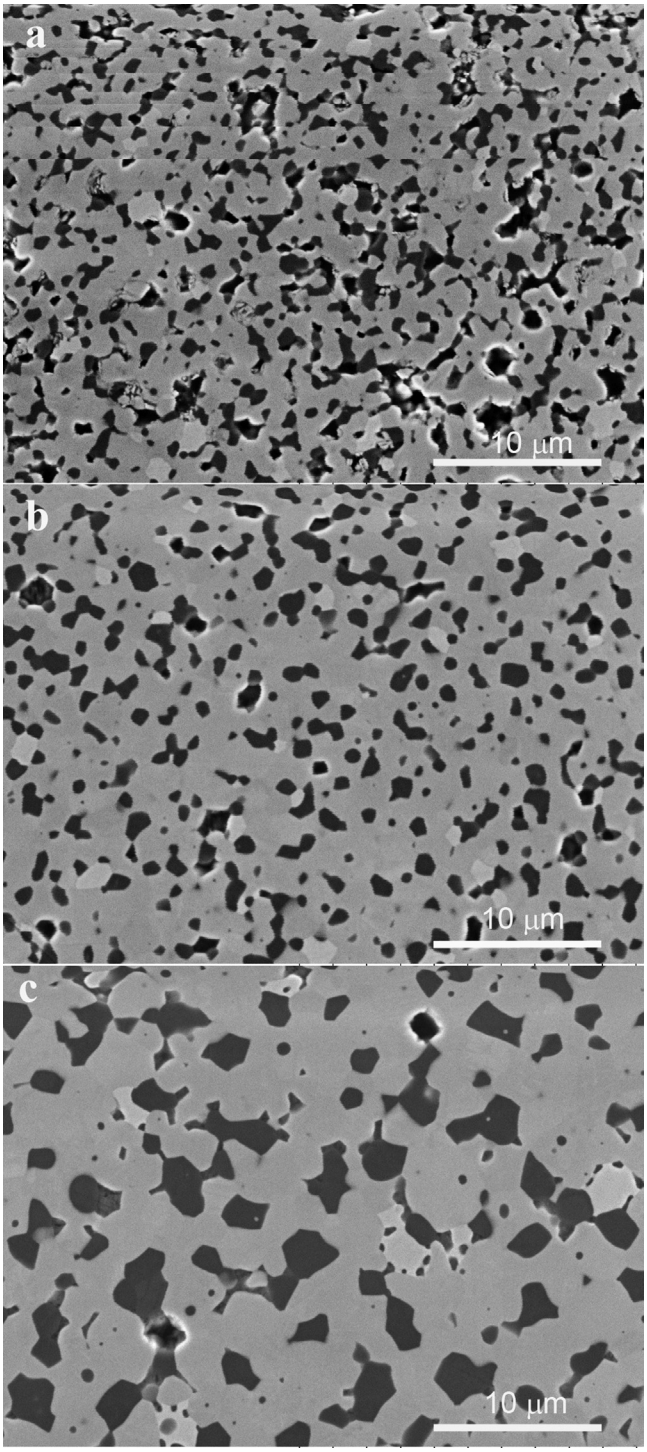

Fig. 7. Characteristic microstructural features of DBZ materials. Detail of the microstructural features observed in Fig. 6. A major medium gray phase, a second dark phase and pores are observed. A minor phase (light gray) is observed at this magnification in all materials. Scanning electron micrographs of "as polished" surfaces. (a) Material sintered at 1350 °C. (b) Material sintered at 1400 °C. (c) Material sintered at 1450 °C.

Density and porosity values are summarised in Table 4. For DBZ, density increased from 1350 to 1400 °C and fully dense materials were obtained for 1400 and 1450 °C isothermal treatments. Trend for DNZ was the opposite; being fully dense the specimens treated at 1350 °C and decreasing density for higher temperatures. Figs. 6 and 7show characteristic microstructural features of DBZ materials. All specimens present homogeneous microstructures and a significant grain growth with the temperature is observed. A major medium gray phase and a second dark phase homogeneously distributed in all materials are observed. Large pores of irregular shape were observed at low magnification in the materials treated at 1350 °C and 1400 °C (Fig. 6b and Fig. 6c) while higher magnification was needed to detect small round pores in the material sintered at the highest temperature (Fig. 7c). In this later, a minor phase (light gray) of 1–3 μm uniformly distributed through the microstructure was also observed (Fig. 6c and Fig. 7c). In the other two DBZ materials, this clearer phase was much smaller (<1 μm) and only observed at high magnification (Fig. 7a, and Fig. 7b).

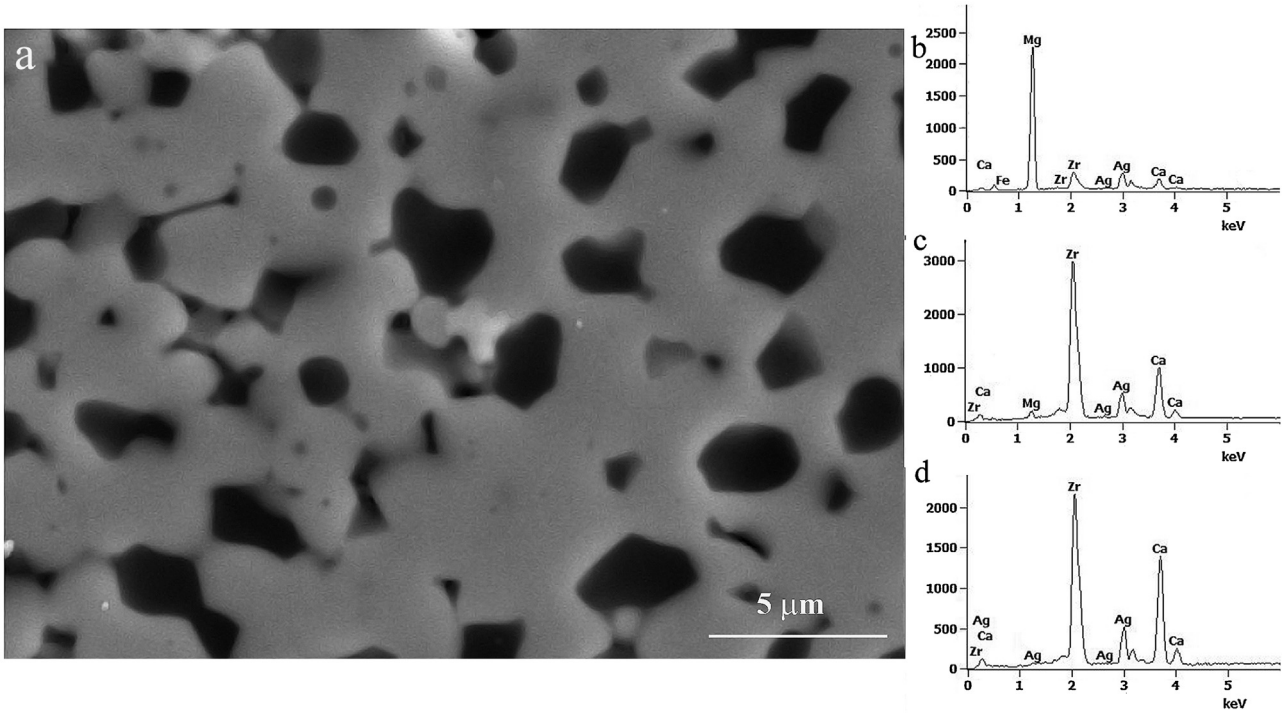

Fig. 8. Chemical composition of the phases present in DBZ materials. b-d: SEM-EDX microanalysis of the different grains in Fig. 8a. (a) Field emission scanning electron micrographs (FE-SEM) of "as polished" surface of material DBZ sintered at 1450 °C. (b) Dark grains: MgO. (c) Light gray small and round grains: c-ZrO_2. (d) Medium gray and faceted grains: $CaZrO_3$.

Table 2
Chemical analysis of the studied compositions calculated taking into account the analysis of the raw materials. Calculations using the complete experimental data as well as simplified compositions calculated in the indicated systems (Z-ZrO_2; C-CaO; M-MgO; S-SiO_2) are provided.

Compound (wt.%)	DBZ				DNZ			
	Experimental	Z-C-M	Z-C-M-S	Z-C-S	Experimental	Z-C-M	Z-C-M-S	Z-C-S
ZrO_2	54.74	55.40	54.93	66.99	54.74	58.31	55.57	66.08
CaO	26.11	26.42	26.20	31.95	23.48	25.01	23.84	28.35
MgO	17.96	18.18	18.02	–	15.66	16.68	15.90	–
SiO_2	0.84	–	0.84	1.03	4.62	–	4.69	5.57
Fe_2O_3	0.05	–	–	–	0.50	–	–	–
$K_2O + Na_2O$	0.10	–	–	–	0.49	–	–	–
Al_2O_3	0.17	–	–	–	0.40	–	–	–
others	0.03	–	–	–	0.10	–	–	–
F + A + S + Alk	1.16		1.2	–	6.01	–	6.1	–

Table 3
Results of the Rietveld refinement for DBZ and DNZ materials sintered at different temperatures. Results from the rational analysis done using the chemical composition (Table 2) and the detected phases is also included.

Crystalline phase content (wt.%)												
T	$CaZrO_3$		c-ZrO_2		MgO		$Ca_3Mg(SiO_4)_2$		$MgCaSiO_4$		Ca_2SiO_4	
(°C)	DBZ	DNZ	DBZ	DNZ	DBZ	DNZ	DBZ	DNZ	DBZ	DNZ	DBZ	DNZ
1350	77.5 ± 0.2	55.7 ± 0.2	1.9 ± 0.03	14.6 ± 0.1	18.1 ± 0.1	13.7 ± 0.2	2.4 ± 0.2	4.5 ± 0.2	–	10.5 ± 0.2	–	0.85 ± 0.2
1400	77.7 ± 0.2	53.5 ± 0.4	1.6 ± 0.03	15.1 ± 0.1	18.0 ± 0.1	15.5 ± 0.5	2.8 ± 0.1	10 ± 0.2	–	2.9 ± 0.2	–	2.5 ± 0.2
1450	75.4 ± 0.5	54.0 ± 0.9	2.2 ± 0.1	17.5 ± 0.5	18.8 ± 0.4	16.2 ± 0.5	3.7 ± 0.3	11.5 ± 1.2	–	–	–	0.66 ± 0.3
Rational analyis	79	55	1	18	18	14	2	13	–	–	–	–

Table 4
Density and porosity values of the studied materials. ρ_{th}: theoretical density. ρ_b: bulk density. RD: relative density. P: porosity.

T(°C)	DBZ				DNZ			
	ρ_{th}(g/cm^3)	ρ_b (g/cm^3)	RD (% of ρ_{th})	P (%)	ρ_{th} (g/cm^3)	P_b (g/cm^3)	RD (% of ρ_{th})	P (%)
1350	4.32	4.07 ± 0.07	93 ± 1	7.0 ± 0.9	4.2	4.25 ± 0.01	100 ± 1	≈0
1400	4.35	4.33 ± 0.08	99 ± 1	≈0	4.2	4.27 ± 0.03	98 ± 1	0.1 ± 0.2
1450	4.36	4.36 ± 0.04	100 ± 1	≈0	4.3	4.20 ± 0.03	97 ± 1	3.0 ± 0.5

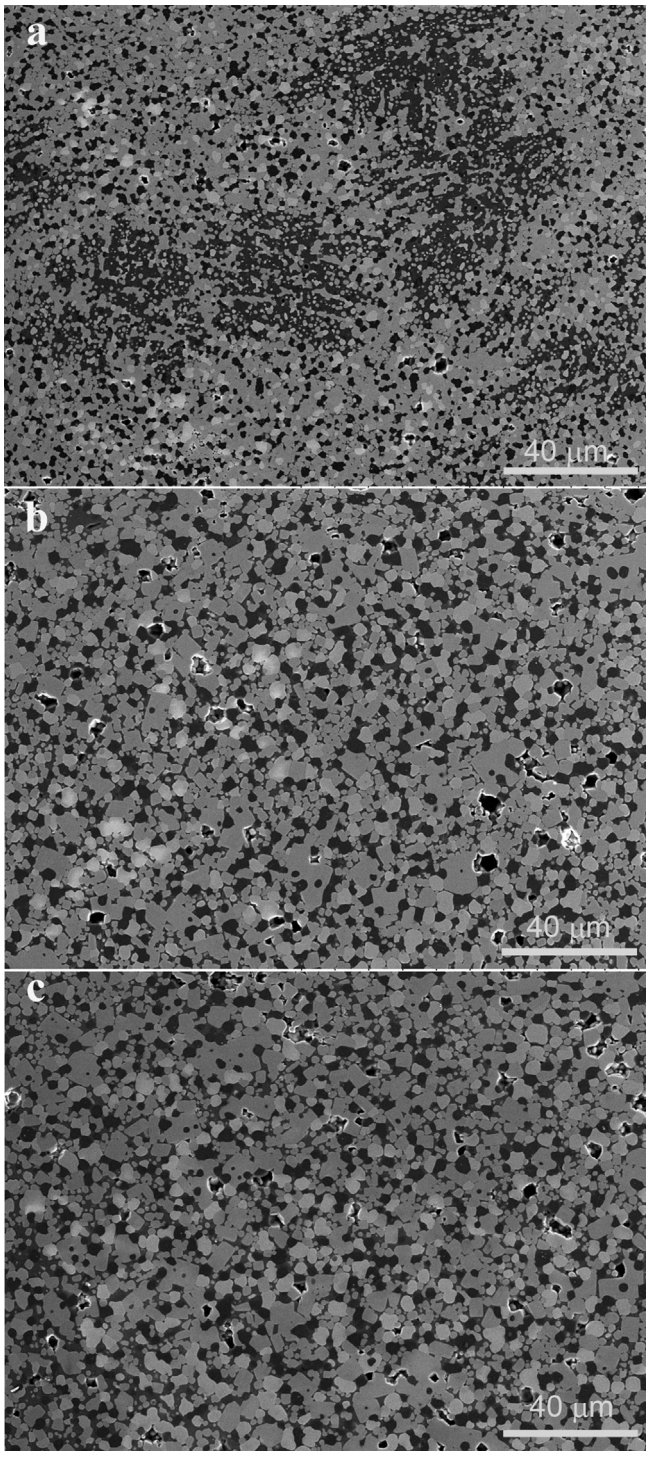

Fig. 9. Characteristic microstructural features of DNZ materials. General aspect of the microstructures observed in scanning electron micrographs of "as polished" surfaces. Common features are: a major medium gray phase, a second dark phase and a minor phase (light gray) and pores (shinny borders). (a) Material sintered at 1350 °C. The dark phase is heterogeneously distributed forming large areas of irregular shape. (b) Material sintered at 1400 °C. (c) Material sintered at 1450 °C.

Characteristic FE-SEM-EDX analyses of particles of the three different grains are shown in Fig. 8 for material sintered at 1450 °C. The composition of the dark grains corresponds to periclase (MgO) and that of the medium gray and faceted grains (CaO ≈31–33 wt.%, ZrO_2 ≈67–69 wt.%) corresponds to $CaZrO_3$. The range of compositions of the light gray smaller and more round particles (ZrO_2 ≈ 77–79 wt.%, CaO: 17–18 wt.%, MgO: 2–4 wt.%) correspond to c-ZrO_2 in which CaO and MgO would enter in solid solution.

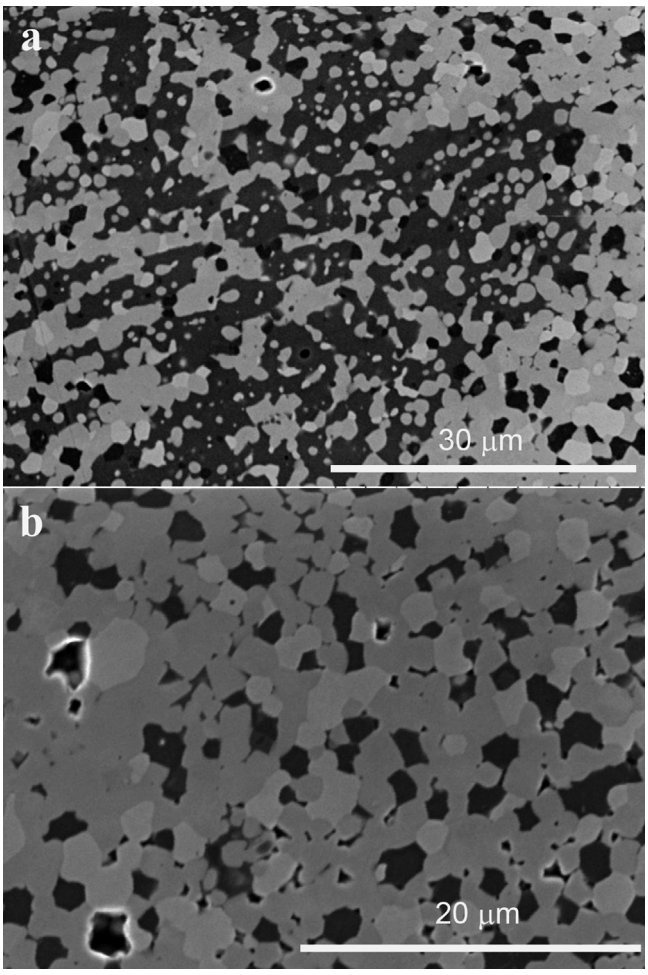

Fig. 10. Details of the microstructural features showed in Fig. 9a, for DNZ materials sintered at 1350 °C. Scanning electron micrographs of "as polished" surfaces. (a) Large dark zones of irregular shape with medium gray particles. (b) Clear areas with particles of three different colours.

Figs. 9–11 show characteristic microstructural features of the DNZ materials. A medium gray major phase, a dark second phase with round black particles embedded, a light gray minor phase and pores were observed in the three materials (Fig. 9). In the material sintered at the lowest temperature, the dark phase was heterogeneously distributed forming large areas of irregular shape (Fig. 9a) with light coloured particles embedded (Fig. 9b). Fig. 10 provides details of the microstructural features showed in Fig. 9a, for DNZ materials sintered at 1350 °C. Fig. 11a show large dark zones of irregular shape with medium gray particles whereas in Fig. 11b clear areas with particles of three different colours are observed. Particles of three different colours—major medium gray phase, second dark phase and minor phase (light gray)—were observed homogeneously distributed in regions out of the dark phase (Fig. 10a and Fig. 11b). Materials sintered at 1400 and 1450 °C (Fig. 11a and Fig. 11b) were homogeneous and a comparison between them shows how the size of the microstructural components increased with temperature.

Fig. 12 shows a detail of the microstructure of the material sintered at 1450 °C together with the characteristic FE-SEM-EDX analyses of the different features. The mineralogy of the different constituents of the microstructure of DNZ materials could also be identified by the combination of EDX and XRD analyses. As in the case of DBZ, the light gray smaller and more round particles were

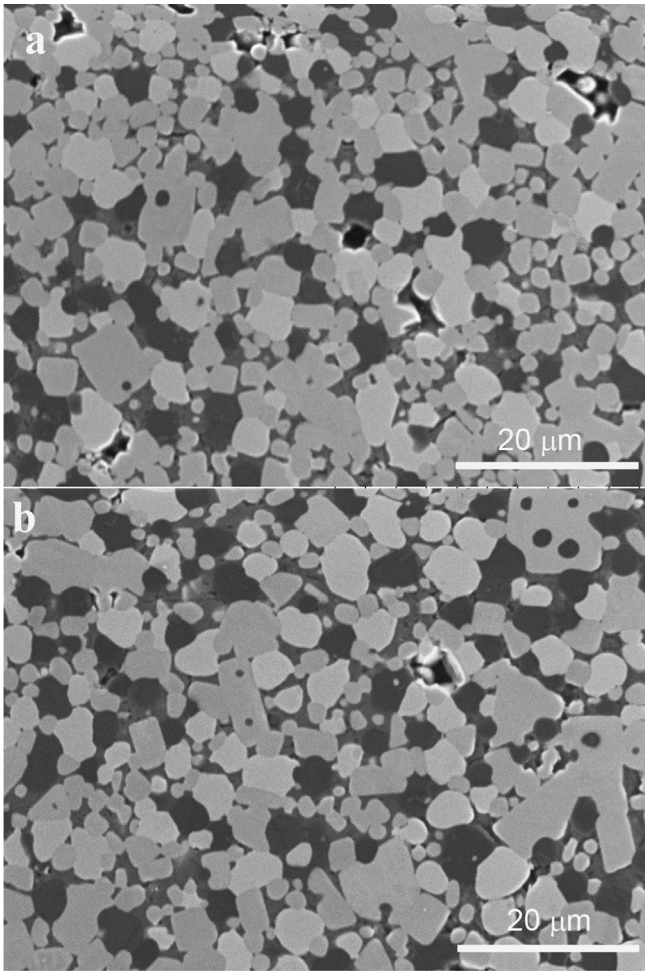

Fig. 11. Details of the microstructural features showed in Fig. 9 for DNZ materials sintered at the highest temperatures. Scanning electron micrographs of "as polished" surfaces. A medium gray major phase, a dark second phase and a minor phase (light gray) and pores (shinny borders) are observed. (a) Material sintered at 1400 °C. (b) Material sintered at 1450 °C.

c-ZrO_2, with CaO and MgO in solid solution. Most of the medium gray and faceted grains were $CaZrO_3$ and it was not possible to differentiate them from those of Merwinite without analyses. In the material sintered at 1350 °C, $Ca_3Mg(SiO_4)_2$ (C_3MS_2), and $CaZrO_3$ particles were mainly found in the dark gray areas (Fig. 11a) and in the clear zones (Fig. 11b), respectively. Black round grains identified as MgO were found embedded in the dark gray continuous phase. This later (probably glassy/amorphous phase) had variable composition according to SEM-EDX microanalysis MgO ≈ 12–14 wt.%, SiO_2 ≈ 37–39 wt.%, CaO ≈ 38–40 wt.% and ZrO_2 ≈ 9–10 wt.%). In the material sintered at 1350 °C, the white particles embedded in the continuous phase were also identified as ZrO_2.

3.3. Mechanical properties

Fig. 13 plots total porosity values (Table 4) and Vickers hardness as a function of sintering temperature. Hardness values for DBZ were always higher than those for DNZ, especially for the materials sintered at the highest temperature. For DBZ (Fig. 13a) there are no significant differences between hardness values of materials sintered at different temperatures while significant decrease in porosity can be observed. In particular, a sharp decrease in porosity is observed from 1350 °C to 1450 °C. Porosity values for DNZ (Fig. 13b) increased with temperature especially from 1400 °C to 1450 °C. There are no significant differences between hardness values of the materials sintered at 1350 °C and 1400 °C, and a sharp decrease is observed for 1450 °C.

Experimental DCDT strength values for both compositions sintered at 1400 °C, together with the Weibull strength distributions (Eq. (3)) calculated using the Weibull parameters calculated from the experimental data are plotted in Fig. 14. Strength values for DBZ were higher than those corresponding to DNZ being the characteristic strengths: σ_0 = 148 MPa and 108 MPa, respectively. While Weibull modulus for DNZ was slightly higher (m = 6.6 and 7.8, for DBZ and DNZ, respectively).

Characteristic features of the fracture surfaces are shown in Fig. 15. No critical defects were found in any of the observed fracture surfaces of DCDT specimens. For both materials fracture was tortuous with numerous fracture planes. No special microstructural features were found in DBZ fracture surfaces (Fig. 15a). In DNZ specimens, regions (≈ 100 μm) with aspect similar to those observed in the polished surfaces of specimens sintered at 1350 °C (Fig. 8a and Fig. 9a) were revealed by fracture (Fig. 15b).

4. Discussion

4.1. Reaction sintering process

The two endothermic peaks associated with significant weight losses observed in the DTA-TG (Fig. 1) correspond to the thermal decomposition of dolomite which occurs by two-step endothermic reactions [19,20] according to Eq. (5) and Eq. (6):

$$MgCa(CO_3)_2 \rightarrow CaCO_3 + MgO + 2CO_2 \quad (5)$$

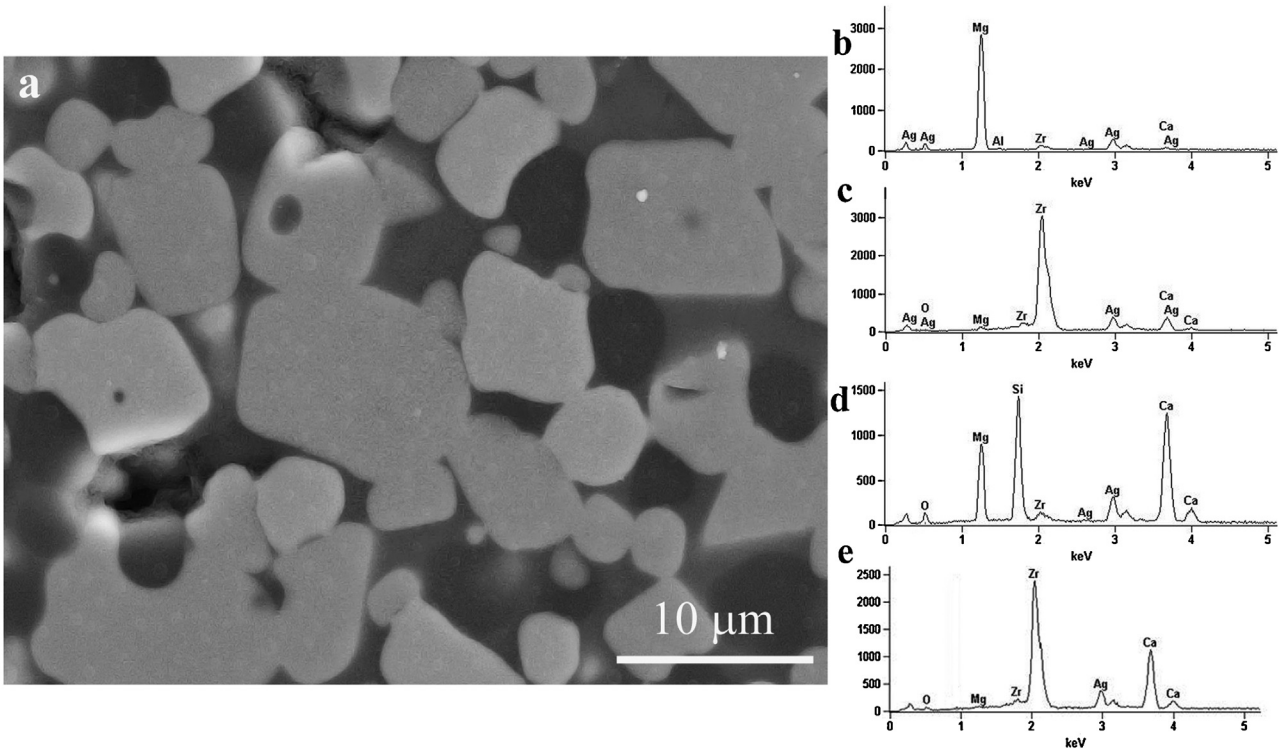

Fig. 12. Chemical composition of the phases present in DNZ materials. b-d: SEM-EDX microanalysis of the different grains in Fig. 12a. (a) Field emission scanning electron micrographs (FE-SEM) of "as polished" surface of material DNZ sintered at 1450 °C. (b) Dark grains: MgO. (c) Light gray small and round grains: c-ZrO_2. (d) Medium gray and faceted grains: $CaZrO_3$. (e) Medium gray and faceted grains: $Ca_3Mg(SiO_4)_3$.

$$CaCO_3 \rightarrow CO_2 + CaO \quad (6)$$

Taking into account the system orthoclase ($KAlSi_3O_8$, melting point at 1150 °C)—Albite ($NaAlSi_3O_8$, melting point at 900 °C), the broad endothermic band with a minimum at about 1100 °C observed in the DTA curve of DN can be attributed to the fusion of the small amounts of alkali feldspars in this material. In the same way, the small endothermic peak at 1320 °C is due to the plagioclase ($(Na,Ca)Al(Si,Al)Si_2O_8$) impurities (system albite $NaAlSi_3O_8$, fusion temperature at 1150 °C)—anortithe ($CaAl_2Si_2O_8$, fusion temperature at 1557 °C) [9,21].

According to the particle size distributions for 4 h milling (Fig. 2), both starting mixtures were relatively fine, with only about 5 vol.% of particles larger than 4 μm. The shift of the largest particles sizes versus small ones reveals the efficiency of milling of the dolomite powders.

Decomposition of dolomite in the milled mixtures starts at lower temperatures (≈200 °C) than in the original raw materials, as reported also by other authors [15]. This fact reveals that dolomite suffers significant structural degradation during milling (Fig. 1 and Fig. 4). The distortion of the dolomite structure induced by grinding in the mixtures of dolomite m-ZrO_2 is reflected by the broadening and shift of the thermal effects (Fig. 1 and Fig. 3), as well as in the reduction of peak intensities of XRD of these samples (not shown). Additional DTA peak centred at 1090 °C for DBZ could be attributed to the formation of the silicates detected by XRD in the sintered DBZ materials (Table 3) as discussed below ($Ca_3Mg(SiO_4)_2$, $CaMgSiO_4$).

According to Serena et al. [15], the formation of $CaZrO_3$ by the solid state reaction between m-ZrO_2 and CaO is described by Eq. (7):

$$CaO + \text{m-}ZrO_2 \rightarrow CaZrO_3 \quad (7)$$

The reaction occurs in a broad temperature range (≈770–1200 °C), thus, there is not a clear endothermic effect observed in the DTA (Fig. 3). Reaction occurs in three steps described by reactions of Eq. (5) to Eq. (7) with extreme large mass losses associated to reactions of Eq. (5) and Eq. (6). Such mass losses result in instabilities observed in the constant shrinkage rate curves (Fig. 4). Before the formation of $CaZrO_3$, both compositions present low shrinkage (≈10–11%), whereas the most significant shrinkage fraction (≈75%) takes place once reactions have finished. Final total shrinkages of the mixtures were ≈40% and 50% for DBZ and DNZ, respectively.

From the above discussion, it is clear that the reaction sintering process of the dolomite-zirconia involves a well differentiated stage of reaction at relatively low temperatures.

In order to reach constant shrinkage, relatively high initial heating rates (5–10 °C/min) were needed for both materials, followed by extremely low rates (0.3–0.4 °C/min) for the final stages of heating. A rate of 2 °C/min, required to follow constant shrinkage rate for DBZ, is an admissible rate for heating small furnaces, such as the laboratory one used. However, heating rates lower than 0.5 °C/min are too low to be imposed. Therefore, a simplified thermal cycle for heating to be used in the furnace for sintering of both composites was established. The heating cycle consisted of three stages of constant heating rates:—first up to 600 °C at 5 °C/min;—second from 600 to 1270 °C at 2 °C/min and the third from 1270 °C to the maximum temperature at 1 °C/min.

4.2. Phase content and microstructure

The microstructures shown in Figs. 6–12 reveal the same crystalline phases as those identified by XRD (Table 3).

A simple rational analysis using the crystalline phases detected by and the chemical composition of the mixtures (Table 2) predicts solid state compositions for DBZ and DNZ consistent with those derived from the Rietveld refinements (Table 3), which supports further the quality of the refinement.

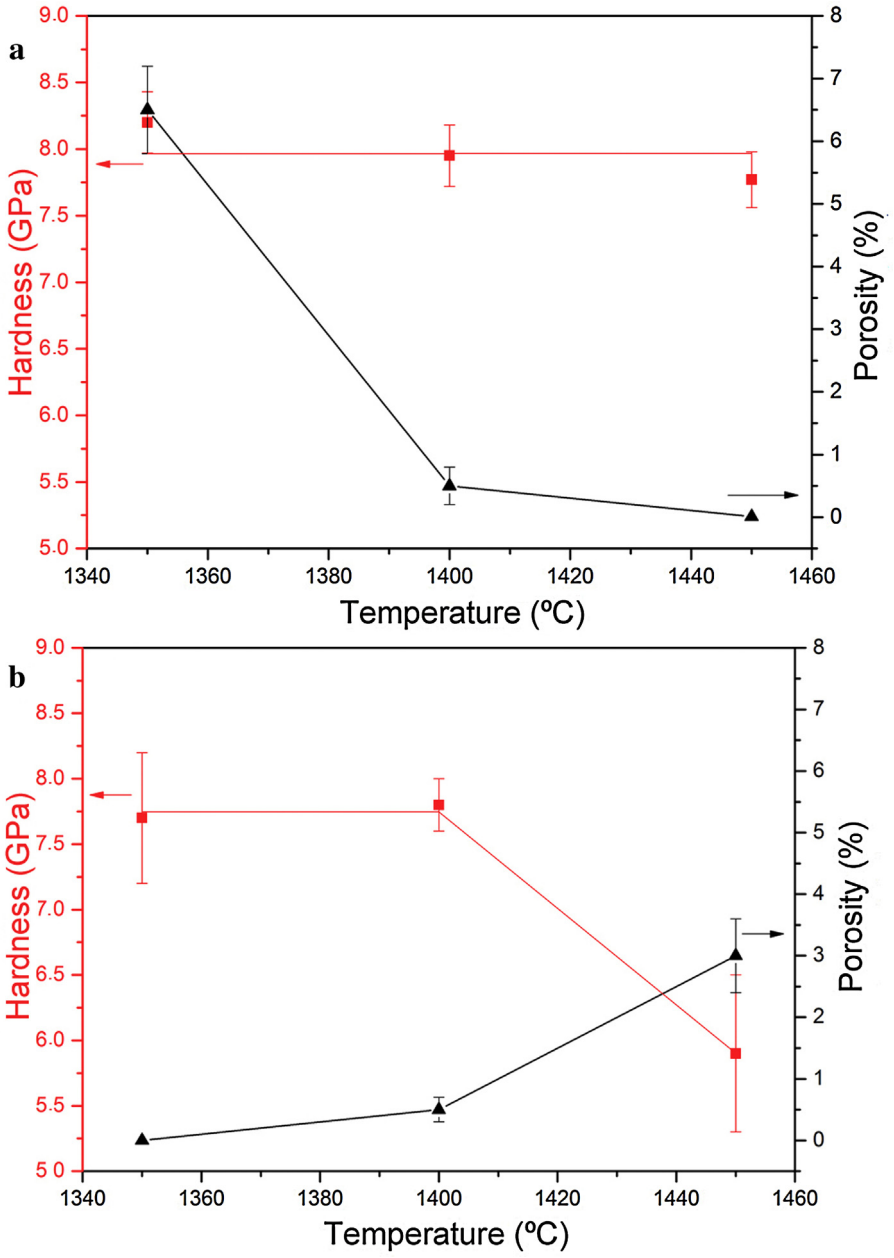

Fig. 13. Porosity values (Table 4) and Vickers hardness as a function of sintering temperature. (a) Materials DBZ. (b) Materials DNZ.

In order to evaluate the potential effect of impurities on the liquid formation, amorphous phases in the specimens sintered at 1400 °C were quantified by Rietveld analysis (Fig. 5c-d). Although the results (4 and 10 wt.% of amorphous phases in DBZ and DNZ, respectively) presented a considerable uncertainty (≈30%), they can be used for the qualitative understanding of differences between DBZ and DNZ materials.

For understanding the mineralogical composition of the sintered specimens of both series of materials it is necessary to consider the equilibrium relationships at the sintering temperature for the compositions corresponding to their chemical analysis (Table 2). As a first approximation, compositions constituted only by the three major components (ZrO_2-CaO-MgO) can be considered. In this system (Fig. 16a) both compositions are located in the primary crystallization field of MgO and very near to the line of solid state compatibility $CaZrO_3$–MgO. The invariant point of this system, 1982 °C [1,2], is well above the treatment temperatures used in this work.

Therefore, pure materials with the stoichiometric compositions (Eqs. (5)–(7)) sintered at 1350–1450 °C would be constituted by $CaZrO_3$ and MgO. The fact that almost no c-ZrO_2 and no CaO were present in DBZ materials after sintering reveals the high degree of reaction reached in these materials, in agreement with all reactions taking place at low temperatures, as previously discussed.

In order to explain the presence of Si-containing minor phases, as well as the large discrepancy between the stoichiometry and the phases present in DNZ, it is necessary to take into account the presence of impurities in DN, which proportion was much higher than in DB (Table 2).

Considering that silica is the main impurity in both dolomites, the quaternary system ZrO_2-CaO-MgO-SiO_2 can be considered for discussion. DBZ and DNZ compositions are located in the formulation plane ([MgO·CaO]-ZrO_2-SiO_2]) of this quaternary

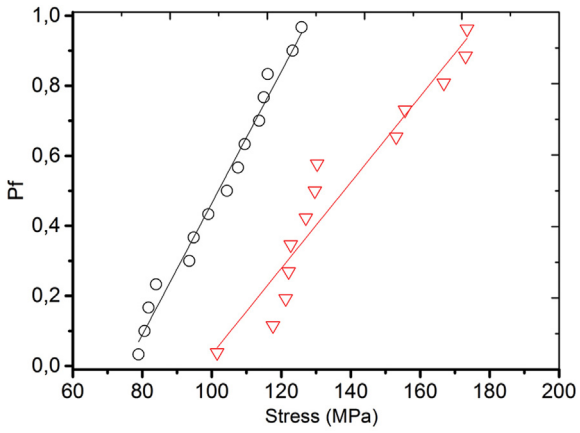

Fig. 14. Weibull plots for materials sintered at 1400 °C. Symbols represent probability of failure, P_f, for the experimental strength values (Eq. (4)). Continuous lines stand for calculations of P_f, using the determined Weibull parameters: Weibull modulus: m = 6.6 and 7.8, for DBZ and DNZ, respectively. Characteristic strength: σ_0 = 148 and 108 MPa, for DBZ and DNZ, respectively.

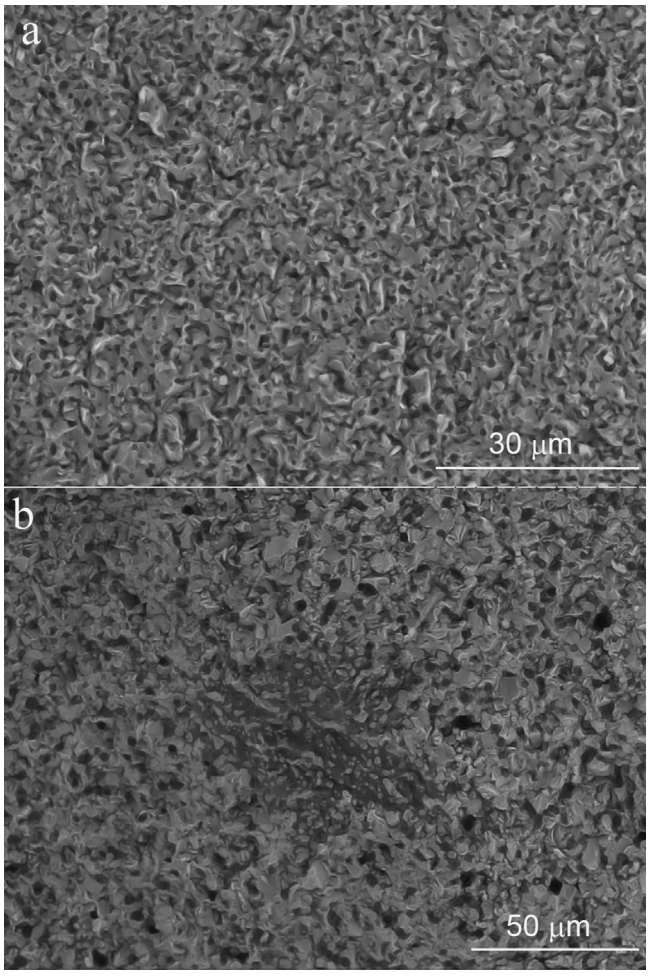

Fig. 15. Characteristic features of the DCDT fracture surfaces of materials sintered at 1400 °C. Scanning electron micrographs. (a) DBZ. (b) DNZ.

(Fig. 16b) and the corresponding solid phases in equilibrium will be MgO–$CaZrO_3$–ZrO_2ss–$Ca_3Mg(SiO_4)_2$. As the invariant point is 1475 °C (peritectic MgO-$CaZrO_3$-cZrO_2-$Ca_3Mg(SiO_4)_2$), pure quaternary compositions treated in the temperature range used in this work will be completely solid.

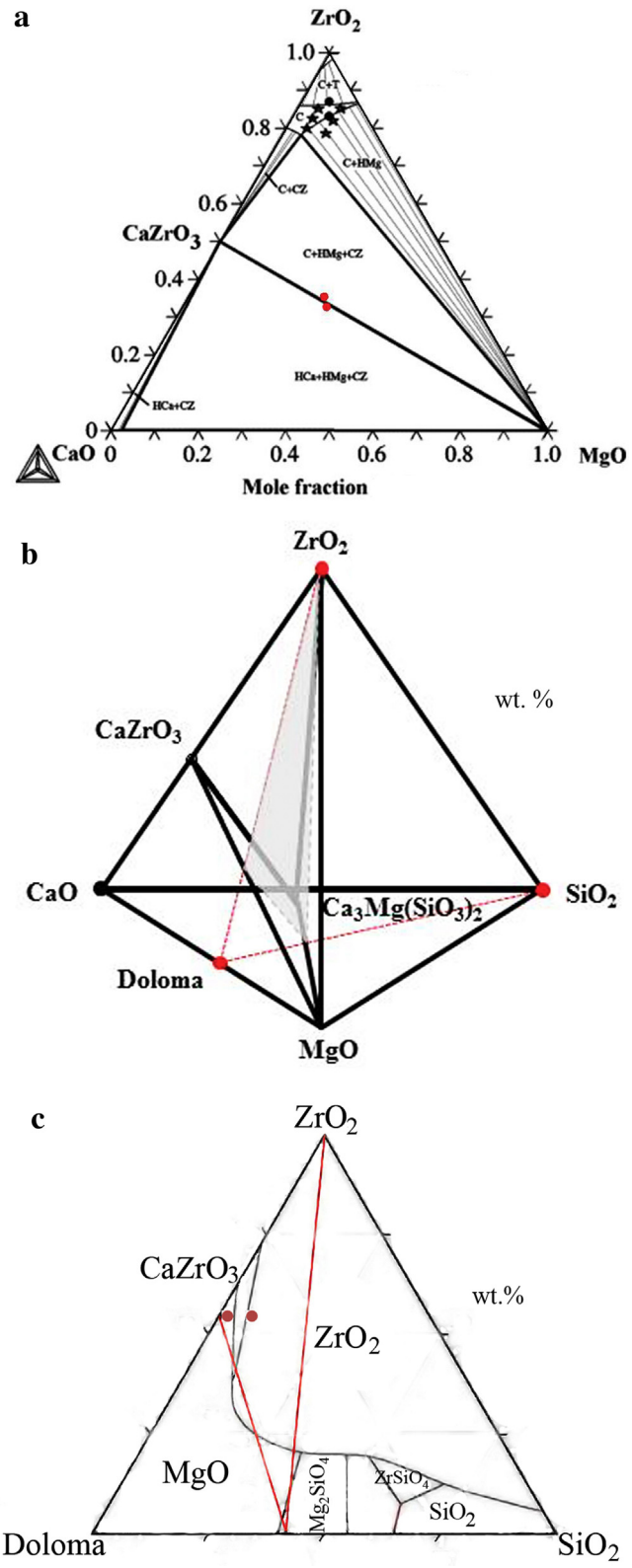

Fig. 16. Phase relations in the quaternary system ZrO_2-CaO-MgO-SiO_2. (a) Phase equilibrium diagram of system ZrO_2-MgO-CaO. The two points mark the studied compositions DBZ and DNZ. (b) Diagrammatic representation of the solid state compatibilities in the formulation plane doloma (CaO·MgO)-ZrO_2 SiO_2. (c) Doloma-zirconia-silica composition plane with the primary composition fields plotted. Note that the DNZ composition is located in the primary crystallization volume of periclase whereas DNZ is located into the zirconia primary volume.

However, due to differences between the chemical compositions of DBZ and DNZ, the composition DBZ is located in the primary phase volume of MgO whereas DNZ is located into the primary phase volume of ZrO_2 (section ZrO_2-[MgO·CaO]-SiO_2, Fig. 16c) [22,23]. Consequently, the differences in the chemical compositions of the natural dolomites used lead to extremely different solid phases after the thermal treatment, as observed (Table 3). Moreover, the composition and amount of liquids that will be formed in quaternary materials with minor impurities will also be different.

Due the presence of impurities, the temperatures of first liquid formation in the studied materials are lower than 1475 °C. These temperatures can be as low as ≈1100 °C, due to the fusion of the very small amounts of alkali feldspars (system orthoclase ($KAlSi_3O_8$, melting point at 1150 °C); albite ($NaAlSi_3O_8$, melting point at 900 °C)) and plagioclase (Na,Ca)Al(Si,Al)Si_2O_8) impurities (system albite ($NaAlSi_3O_8$, melting point at 1150 °C); anortithe ($CaAl_2Si_2O_8$, melting point at 1557 °C) [21].

Slight amounts of liquid can be responsible for the high density reached by DBZ specimens, in which pore closure and disappearance occurred at 1400 °C and 1450 °C, respectively (Table 4, Figs. 6–7b-c). Increased material transport due to the presence of liquid was also responsible for the appreciable grain growth at 1450 °C (Figs. 6–7c).

The large amounts of liquid, identified as the dark gray continuous phases with variable compositions, formed in DNZ promoted the swelling of the specimens, with the associated decrease in density as temperature increased (Table 4). Additionally, the presence of significant amounts of liquid led to the devitrification of non-equilibrium phases, such as $MgCaSiO_4$ and Ca_2SiO_4 (Table 3), during cooling from the sintering temperature.

In order to evaluate the potential use of the studied materials in structural applications at high temperature, it is necessary to consider the characteristics of the liquids formed. The composition of the quaternary liquid at the peritectic invariant point can be estimated taking into account the compositions of the projections of this peritectic from the apex of MgO [24–26] and ZrO_2 [26,27]. The calculated composition (MgO: 13 wt.%; SiO_2: 38 wt.%; CaO: 40 wt.%; ZrO_2: 9 wt.%) is similar to the quaternary compositions identified by SEM-EDX in the dark gray continuous (Fig. 12, MgO ≈ 12–14 wt.%, SiO_2 ≈ 37–39 wt.%, CaO ≈ 38–40 wt.% and ZrO_2 ≈ 9-10). Taking into account these compositions, there will not be differences between the behaviour of the liquids formed in the two studied materials.

High silica and zirconia liquids, as those discussed above, are known to have high viscosity [13,18,28]. Moreover, Karell et al. [29–31] reported that increasing content of ZrO_2 substituting SiO_2 in the glass network increases the values of glass transition temperature and viscosity. The fact that swelling occurred in DNZ specimens was due to the presence of additional impurities, as revealed by the multicomponent liquids identified (Fig. 12).

4.3. Mechanical properties

Hardness of the materials is determined by the phase composition and the porosity. In general increasing amounts of porosity and/or glass involves a decrease of hardness. In DBZ materials, these two microstructural characteristics presented inverse trends with temperature and therefore, the characteristic increase in hardness as porosity decreases was not observed in this family of materials (Fig. 13a). For DNZ, porosity values together with glass content increased with temperature leading to a significant hardness decrease (Fig. 13b).

DBZ and DNZ composites sintered at 1400 °C have similar porosity. However, DBZ composites attained higher hardness and strength when compared with DNZ composition. The lower glass content together with finer microstructure in DBZ (Figs. 8, 12 and 14) would be responsible for the improved mechanical behaviour of this material.

Due to the thermal expansion mismatch between $CaZrO_3$ (large thermal expansion anisotropy ($\alpha_a = 4.9 \times 10^{-6}\,K^{-1}$, $\alpha_b = 10.9 \times 10^{-6}\,K^{-1}$, $\alpha_c = 15.1 \times 10^{-6}\,K^{-1}$), average $\alpha = 10.4 \times 10^{-6}\,K^{-1}$) and MgO ($13.5 \times 10^{-6}\,K^{-1}$) thermal stresses should be expected in these composites during the cooling process. Such stresses would be responsible for the tortuous fracture surfaces with different fracture planes observed for both composites (Fig. 15). Residual stresses can promote the development of micro cracks leading to a potential increase in toughness and thermal shock resistance of the studied materials.

5. Conclusions

Dense $CaZrO_3$–MgO based composites with fine microstructure were obtained by reaction sintering of attrition milled mixtures of dolomite and ZrO_2 (molar ratio 1:1). Complete reaction was attained at 1350 °C. Two dolomites with different levels of impurities were used to fabricate the materials: high purity (impurity content ≈1.2 wt.%, material DBZ) and impure dolomite (impurity content ≈6.12 wt.%, material DNZ).

Phase composition was highly dependent on impurities in the natural dolomites used. Main differences were the amount of c-ZrO_2 and the nature and amount of secondary phases.

The materials obtained using the low purity dolomite presented higher glass content and larger microstructure that were responsible for lower hardness and strength than those of the high purity materials. Moreover, liquids formed in these materials will present low viscosity at low temperature (≈1400 °C) due to the minor impurities, restraining the use of DNZ materials in structural applications of responsibility.

The low amounts of liquid formed in the purest materials, DBZ, with lower proportions of minor impurities and higher contents of ZrO_2, will present high transition temperatures and viscosities. Therefore, DBZ materials could be proposed for structural applications at temperatures up to 1450 °C. This work has clearly demonstrated that natural raw materials can be used to fabricate materials for structural applications of responsibility if the nature and content of impurities is carefully controlled.

Acknowledgements

This work was performed in the frame of the CYTED network HOREF (312RT0453).

Abílio Silva acknowledges the support from thePortuguese national funding agency: FCT—Fundação para a Ciência e a Tecnologia, through the grant: SFRH/BSAB/105760/2014, and also acknowledges Instituto de Cerámica y Vidrio, ICV-CSIC, Madrid, Spain for an invited research stage.

References

[1] S. Serena, M.A. Sainz, A. Caballero, Experimental determination and thermodynamic calculation of the ZrO_2-CaO-MgO system at 1600°, 1700°, and1750 °C, J. Am. Ceram. Soc. 87 (12) (2004) 2268–2274.
[2] S. Serena, M.A. Sainz, S. De Aza, A. Caballero, Thermodynamic assessment of the system ZrO_2–CaO–MgO using new experimental results: calculation of the isoplethal section MgO-CaO–ZrO_2, J. Eur. Ceram. Soc. 25 (5) (2005) 681–693.
[3] M.D. Mathews, E.B. Mirza, A.C. Momin, High temperature X-ray diffractometric studies of $CaZrO_3$, $SrZrO_3$ and $BaZrO_3$, J. Mater. Sci. Lett. 10 (1991) 305–306.
[4] P.S. Murti, M.V. Krishnaiah, Investigation of the thermal conductivity calcium zirconate, Mater. Chem. Phys. 31 (1992) 347–350.
[5] S.P. Terblanche, Thermal-expansion coefficients of yttria-stabilized cubic zirconias, J. Appl. Cryst. 22 (1989) 283–284.
[6] M.R. Winter, D.R. Clarke, Thermal conductivity of yttria-stabilized zirconia–hafnia solid solutions, Acta Mater. 54 (2006) 5051–5059.

[7] A. De Petris, F. Ricciardiello, O. Sbaizero, Mechanical properties of polycrystalline $CaZrO_3$, Powder Metall Int. 18 (1986) 427–443.
[8] C. Cano, M.I. Osendi, M. Belmonte, P. Miranzo, Effect of the type of flame on the microstructure of $CaZrO_3$ combustion flame sprayed coatings, Surf. Coat. Tech. 201 (2006) 3307–3313.
[9] S.K. Durrani, A.H. Qureshi, S. Naz, S.Z. Hussain, M. Arif, M. Iqbal, Effect of stoichiometric compositions on the development of phase and microstructure in calcia stabilized zirconia ceramic, Nucleus 50 (1) (2013) 61–66.
[10] W.E. Lee, W.M. Rainforth, Refractory materials, in: Ceramic Microstructures: Property Control by Processing, Chapman & Hall, London, UK, 1994, pp. 470–488.
[11] A.J. Slifka, B.J. Filla, J.M. Phelps, Thermal conductivity of magnesium oxide from absolute: steady-state measurements, J. Res. Natl. Inst. Stand. 103 (4) (1998) 357–363.
[12] S. Serena, M.A. Sainz, A. Caballero, Neutron thermodiffractometry study of calcium zirconate/magnesium oxide formation in the ZrO_2-CaO-MgO, J. Am. Ceram. Soc. 87 (2004) 1706–1713.
[13] J. Szczerba, Z. Pedzich, The effect of natural dolomite admixture on calcium zirconate-periclase materials microstructure evolution, Ceram. Int. 36 (2010) 535–547.
[14] R. Angers, R. Tremblay, A.C. Chaklader, Formation of $CaZrO_3$ by solid-state reaction between CaO and ZrO_2, J. Amer. Ceram. Soc. 55 (8) (1972) 425–426.
[15] S. Serena, A. Caballero, M.A. Sainz, Analysis of the polymorphic transformation of nano- and microcrystalline zirconia doped with CaO and MgO during reaction-sintering process by neutron thermodiffraction. A thermodynamic approach, J. Eur. Ceram. Soc. 33 (2013) 1413–1424.
[16] O.B. Zgalat-Lozinskii, Nanostructured materials nanocomposites based on refractory compounds, consolidated by rate-controlled and spark-plasma sintering (review), Powder Metall Met C+ 53 (2014) 19–30 (Russian Original Vol. 53: 1-2, Jan.-Feb., 2014).
[17] A.V. Ragulya, Rate-controlled synthesis and sintering of nanocrystalline barium titanate powder, Nanostruct. Mater. 10 (3) (1998) 349–355.
[18] I.H. García-Páez, R. García-Carrodeguas, A.H. De Aza, C. Baudín, P. Pena, Effect of Mg and Si co-substitution on microstructure and strength of tricalcium phosphate ceramics, J. Mech. Behav. Biomed. Mater. 30 (2014) 1–15.
[19] R. Otsuka, Recent studies on the decomposition of the dolomite group by thermal analysis, Thermochim. Acta 100 (1) (1986) 69–80.
[20] A.H. De Aza, M.A. Rodriguez, J.L. Rodriguez, S. De Aza, P. Pena, P. Convert, T. Hansen, X. Turrillas, Decomposition of dolomite monitored by neutron thermodiffractometry, J. Am. Ceram. Soc. 85 (2002) 881–888.
[21] O.F. Tuttle, N.L. Bowen, System Na_2O-CaO-Al_2O_3-SiO_2. Phase diagrams for ceramist, 1 (1950) (Fig. 00833.).
[22] J.L. Rodriguez Galicia, Materiales De Magnesia Circonato cálcico Obtenidos Por Sinterización Reactiva De Mezclas De Dolomita-circón, (Ph.D. Thesis), Autonomous University of Madrid, 2001 (in Spanish language).
[23] J.L. Rodriguez, C. Baudín, P. Pena, Relationships between phase constitution and mechanical behaviour in MgO-$CaZrO_3$-calcium silicate materials, J. Eur. Ceram. Soc. 24 (2004) 669–679.
[24] S. De Aza, C. Richmond, J. White, Compatibility relationships of periclase in the system CaO-MgO-ZrO_2-SiO_2, Trans. J. Br. Ceram. Soc. 73 (4) (1974) 109–116.
[25] A. Sircar, N.-H. Brett, J. White, Phase studies in the system CaO-MgO-ZrO_2-SiO_2 part I- compatibility relationships of periclase, Trans. J. Br. Ceram. Soc. 77 (1978) 70–78x.
[26] P. Pena, B. Vázquez, A. Caballero, S. De Aza, Quaternary phase equilibrium diagrams: representation and interpretation methods, Bol. Soc. Esp. Ceram. Vidr. 44 (1) (2005) 113–122.
[27] A. Sircar, N.-H. Brett, J. White, Phase studies in the system CaO-MgO-ZrO_2-SiO_2 part II- compatibility relationships of zirconia, Trans. J. Br. Ceram. Soc. 78 (3) (1979) 77–88.
[28] S. Serena, M.A. Sainz, A. Caballero, The system Clinker–MgO–$CaZrO_3$ and its application to the corrosion behavior of $CaZrO_3$/MgO refractory matrix by clinker, J. Eur. Ceram. Soc. 29 (2009) 2199–2209.
[29] R. Karell, J. Kraxner, M. Chromcikova, Properties of selected zirconia containing silicate glasses, Ceram-Silikaty 50 (2) (2006) 78–82.
[30] R. Karell, J. Kraxner, M. Chromcikova, M. Liska, Properties of selected zirconia containing silicate glasses II, Ceram-Silikaty 51 (3) (2007) 125–130.
[31] R. Karell, M. Chromcikova, M. Liska, Properties of selected zirconia containing silicate glasses III, Ceram-Silikaty 52 (2) (2008) 102–108.